JGR Space Physics

RESEARCH ARTICLE
10.1029/2020JA028695

Key Points:

- The long-term variations in the geomagnetic activity and the solar wind-magnetosphere coupling are studied
- The geomagnetic activities of different types exhibit varying solar cycle dependencies
- The weak solar cycles are associated with the reduced solar wind-magnetosphere coupling and geomagnetic activity

Correspondence to:
R. Hajra,
rajkumarhajra@yahoo.co.in

Citation:
Hajra, R., Marques de Souza Franco, A., Echer, E., & Bolzan, M. J. A. (2021). Long-term variations of the geomagnetic activity: A comparison between the strong and weak solar activity cycles and implications for the space climate. *Journal of Geophysical Research: Space Physics*, *126*, e2020JA028695. https://doi.org/10.1029/2020JA028695

Received 10 SEP 2020
Accepted 28 FEB 2021

Long-Term Variations of the Geomagnetic Activity: A Comparison Between the Strong and Weak Solar Activity Cycles and Implications for the Space Climate

Rajkumar Hajra[1], Adriane Marques de Souza Franco[2], Ezequiel Echer[2], and Mauricio José Alves Bolzan[3]

[1]Indian Institute of Technology Indore, Indore, India, [2]Instituto Nacional de Pesquisas Espaciais (INPE), São José dos Campos, Brazil, [3]Federal University of Jatai, Jatai, Brazil

Abstract We study the long-term variations of geomagnetic activity using more than five solar cycles of geomagnetic and solar wind observations. From the Dst index variation, 1523 geomagnetic storms were identified during January 1957 through December 2019, and 145 high-intensity long-duration continuous auroral electrojet (AE) activity (HILDCAA) events were identified using the AE index from January 1975 through December 2017. Among the storms, ∼3/4th were moderate (−50 nT ≥ Dst > −100 nT), and only ∼1/4th were stronger in intensity (Dst ≤ −100 nT). Cross-correlation analysis reveals a strong correlation (r = 0.58−0.78) between the magnetic storms and the F10.7 solar flux at 0−1-year time lag and a weaker correlation (r = 0.59) between HILDCAAs and F10.7 at a ∼3-year lag. This result is consistent with the magnetic storm occurrence rate centered around the solar cycle maximum with a secondary peak after the maximum, and HILDCAAs peaking around the descending phase. Wavelet analysis reveals a dominating ∼10–11-year periodicity in the number of geomagnetic storms and HILDCAAs, geomagnetic activity indices, solar wind, and interplanetary parameters. The periodicity is attributed to the solar activity cycle variation. Solar wind speed induces additional longer (∼15−16 years) and shorter (∼3−5 years) scale variations in geomagnetic activity. Solar cycles 20 and 24 are found to be significantly weaker compared to the cycles 19, 21, 22, and 23 in solar flux, solar wind-magnetosphere coupling, and resultant geomagnetic activity. If the decreasing trend of the solar and geomagnetic activities continues in cycle 25, this may have important implications for the space weather science and operations.

1. Introduction

A large percentage of modern technical systems, from space communication satellites to ground-based power grids, is vulnerable to space weather (see Cannon et al., 2013; Lakhina et al., 2020, and references therein). Space weather includes everything from variations in the Sun, solar wind to their impacts on the interplanetary space, Earth, and other solar system bodies with varying magnetic and plasma properties (e.g., Echer et al., 2005; Hajra et al., 2020, and references therein). These are strongly modulated by the ∼11-year "Schwabe" cycle (Schwabe, 1844) when Sun's activity rises and falls. In addition to this oscillation, solar activity is reported to exhibit longer-scale modulations such as ∼80–90-year variation in the cycle amplitudes (Gleissberg, 1939), known as Gleissberg cycle (see Hathaway, 2015, for an excellent review on this topic). The long-term study of the space weather over time scales of several solar cycles is important for the knowledge of space climate (e.g., González Hernández et al., 2014; Mursula et al., 2007), which is the main focus of this present work.

The solar wind-magnetosphere coupling and its relationship to geomagnetic disturbances are the most important aspects of the space research. The energy coupling process is mainly controlled by magnetic reconnection between the dayside geomagnetic field and interplanetary magnetic field (IMF) (Dungey, 1961). In this process, the northward geomagnetic field lines break upon encounter/contact with the (antiparallel) southward IMF in the dayside magnetopause current sheet where magnetic diffusion is significant. The "open" geomagnetic field lines connected with the IMF are transported down-tail across the polar cap by the solar wind flow and again reconnect at the far tail current sheet region. It may be mentioned that in the "closed magnetosphere" under northward IMF, the solar wind-magnetosphere energy coupling through

viscous interaction (Axford & Hines, 1961) is comparatively less efficient (Gonzalez et al., 1994; Tsurutani, Gonzalez, Tang, & Lee, 1992).

An enhanced energy transfer for a long period of stronger magnetic reconnection leads to the enhancement of the energetic (~10–300 keV) ring current particles (mainly H^+, O^+, He^+, and electrons) at ~2–7 Earth radii (R_E) in the Earth's magnetic equatorial plane (Daglis et al., 1999; Frank, 1967; Hamilton et al., 1988; Singer, 1957; Williams, 1987, and references therein). This may cause global-scale geomagnetic disturbances, commonly known as geomagnetic storms (Chapman & Bartels, 1940; Gonzalez et al., 1994). On the other hand, a low rate magnetic reconnection for an intermittent interval may lead to the precipitation of ~10–100 keV electrons and ions in the auroral atmosphere resulting in auroral substorms (Akasofu, 1964; Nykyri et al., 2019; Ohtani, 2001; Tsurutani & Meng, 1972). Intense auroral substorms continuing for a few days to a week without occurrence of any major geomagnetic storms have been called high-intensity long-duration continuous auroral electrojet (AE) activities (HILDCAAs: Hajra et al., 2013, 2014; Tsurutani & Gonzalez, 1987). These are different from the nominal substorms and major geomagnetic storms.

In the present work, updated lists of geomagnetic storms and HILDCAAs will be developed using all available geomagnetic indices to study their long-term variations. The solar and interplanetary drivers of the long-term geomagnetic activity variations will be explored in order to identify the physical processes associated with the solar wind-magnetosphere energy coupling. The strong and weak solar cycles will be compared in terms of their solar wind and geomagnetic properties. Thus, the main questions to be addressed in this work are: what are the climatological features of the geomagnetic activity and what are the drivers of the space climate? Is there any difference in the geomagnetic characters between the weak and strong solar cycles? What does the current weak solar cycle imply in view of future solar cycles? While some of the questions are already addressed, the present work is statistically much more robust and complete because of very long and updated data sets of HILDCAAs and magnetic storms compared to previous works. Such a long-term study is important for augmentation of our knowledge of the trends in space weather over solar cycles, or the space climate.

2. Database and Method of Analysis

2.1. Geomagnetic Storms and HILDCAAs

Geomagnetic storms are characterized by enhanced westward ring currents (encircling the Earth's magnetic equator) at ~2–7 R_E that lead to decreases in the low-latitude geomagnetic fields. The decreases are measured by the disturbance storm time or Dst index. The Dst index is derived from the horizontal magnetic field measurements by four magnetometers placed around the Earth's magnetic equator (Burton et al., 1975; Sugiura, 1964). The measurements are continuously available from January 1957. Using the usual storm criteria Dst ≤ −50 nT (Gonzalez et al., 1994), we identified 1523 magnetic storms from January 1957 through December 2019. This updated list of storms in fact extends and complements the previously developed lists of storms between 1957 and 2008 (Echer et al., 2011) and storms occurring in solar cycle 24 till 2016 (Rawat et al., 2018).

Figure 1 shows the distribution of the magnetic storms binned according to the peak Dst values. An approximate exponential decay in the number of storms with the increasing Dst strength can be noted (shown by a solid curve). This implies a very low occurrence probability of the extreme storms. It is interesting to note that while the exponential curve fits well with the bulk storm distribution, the fitting is not efficient for the extreme storms. This is consistent with a similar behavior of the solar wind plasma and IMF (see, e.g., Tsurutani et al., 2018). The median of the storm peak Dst distribution is about −74 nT while the average (standard deviation) is about −92 nT (±54 nT). As the median divides a probability occurrence distribution in halves, it is concluded that about half of the storms are weaker than −74 nT. Among the 1523 storms, ~73% were moderate (−50 nT ≥ Dst > −100 nT), ~24% were intense (−100 nT ≥ Dst > −250 nT), and ~3% were super storms (Dst ≤ −250 nT). This storm strength distribution is shown by a pie chart in Figure 1 (inset). Thus, ~3/4th of the storms were moderate and only ~1/4th were stronger. The moderate storms have an average (median) intensity of ~−68 nT (~−65 nT) with a standard deviation of ±14 nT, the intense storms have an average (median) intensity of ~−140 nT (~−129 nT) with a standard deviation of ±35 nT, and the super storms have an average (median) intensity of ~−325 nT (~−303 nT) with a standard

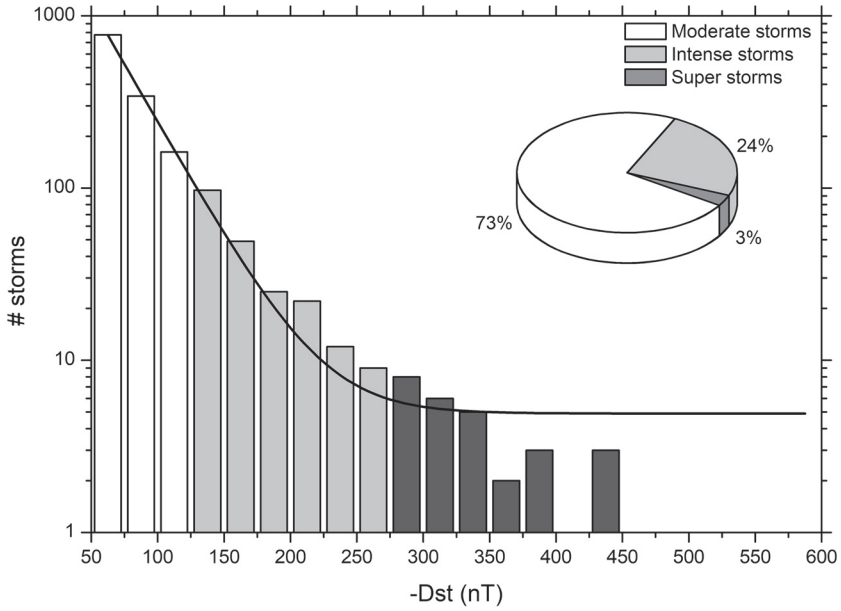

Figure 1. Histograms show the occurrence probability distribution of the peak Dst values of the storms under present study. The solid curve shows the exponential fit. Pie chart in the inset shows the percentage occurrences of the moderate, intense, and super storms.

deviation of ± 69 nT. The standard deviations are ∼20%, ∼25%, and ∼21% of the average storm intensities for the moderate, intense, and super storms, respectively. This implies a large variation in intensity among each category of the storms.

HILDCAAs are identified, using four criteria suggested by Tsurutani and Gonzalez (1987), as the intervals of intense auroral activity with the peak AE intensity >1000 nT, the minimum duration of 2 days when AE does not fall below 200 nT for more than 2 h at a time. These may occur under a non-storm condition (Dst > −50 nT) or during the recovery phase of a geomagnetic storm. Hajra et al. (2013) developed a list of 133 HILDCAA events from January 1975 (1 min AE data are available from January 1975 on) to December 2011. We updated the list to include recent events till end of 2017. Thus, the present work includes 145 HILDCAA events from January 1975 to December 2017.

In addition to the yearly occurrence rates of HILDCAAs and magnetic storms, the average geomagnetic environment is characterized by the yearly averages of the geomagnetic indices Dst, ap and AE. In general, Dst represents a proxy measurement of the storm time ring current (Sugiura, 1964), AE is a proxy of the auroral electrojet current related to substorms (Davis & Sugiura, 1966), and the ap index is an indicator of the global-scale geomagnetic activity level (Rostoker, 1972).

2.2. Solar Wind-Magnetosphere Coupling

The solar wind-magnetosphere coupling during the geomagnetic activity enhanced intervals is explored by the study of the solar wind plasma and IMF parameter variations. We estimated the yearly percentage of days with the daily peak solar wind speed Vsw of ≥500 km s^{-1} (mentioned as D500 in this work) as an indicator of the solar wind high-speed streams (HSSs). We estimated the solar wind electric field VBs, where V represents Vsw, and Bs is the southward component of the IMF (Bs is zero in absence of a southward component). VBs has been shown to take an important role in driving the geomagnetic activity (e.g., Burton et al., 1975; Finch et al., 2008; Tsurutani, Gonzalez, Tang, Lee, et al., 1992). Another important coupling function is the Akasofu ϵ-parameter ($\sim VswBo^2\sin^4(\theta/2)R_{CF}^2$) that gives an approximate estimate of the magnetospheric energy input rate (Perreault & Akasofu, 1978). Here, Bo is the magnitude of the IMF, θ is the IMF orientation clock angle, and R_{CF} is the Chapman-Ferraro magnetopause distance (Chapman & Ferraro, 1931; Shue & Chao, 2013).

2.3. Cross-Correlation Analysis

To study the relationship between the geomagnetic activity and the solar wind-magnetosphere coupling, we use the classical cross-correlation analysis (Davis, 2002). The cross-correlation between two time series is computed by displacing one time series relative to the other in time (t) units. Thus, the successive lags and correlation coefficients, and the lag corresponding to the maximum correlation between the two series can be obtained. A zero lag corresponds to the correlation coefficient (linear correlation) where the time series are aligned. The cross-correlation coefficient (r) between the time series Y_1 and Y_2 with n overlapped positions is defined as:

$$r = \frac{n * \sum Y_1 Y_2 - \sum Y_1 \sum Y_2}{\sqrt{\left[n * \sum Y_1^2 - \left(\sum Y_1\right)^2\right]\left[n * \sum Y_2^2 - \left(\sum Y_2\right)^2\right]}} \quad (1)$$

It varies from −1 to 1 and provides the information of how well the two series are correlated. When r is equal to zero, no correlation exists between the two series. For a positive r, the correlation is positive, which is the maximum for $r = 1$; whereas a negative r means anti-correlation, and a perfect anti-correlation occurs for $r = -1$.

2.4. Wavelet and Cross-Wavelet Analysis

The interplanetary and magnetospheric environments are complex and turbulent with non-stationary variations in their parameters (Souza et al., 2016; Marques de Souza et al., 2018). The wavelet transform (WT) is used to study the temporal variability of the power spectral density in such media (Morettin, 2014). The wavelet functions $\psi(t)$ are generated by a wavelet-mother function shown in Equation 2, which suffers an expansion: $\psi(t) \rightarrow \psi(2t)$, and a translation: $\psi(t) \rightarrow \psi(t+1)$ in time, resulting in wavelet-daughter functions (Torrence & Compo, 1998):

$$\psi_{a,b}(t) = \frac{1}{\sqrt{a}}\psi\left(\frac{t-b}{a}\right), \quad \text{for } a,b \in \mathbb{Z}, \text{and } a \neq 0 \quad (2)$$

In the above equation, a represents the scale associated to the expansion and contraction of the wavelet, and b is the temporal location, related to the translation in time. The WT applied on $f(t)$ time series is defined as:

$$WT(a,b) = \int f(t)\psi^*_{a,b}(t)dt, \quad (3)$$

where $\psi^*_{a,b}(t)$ represents the complex conjugate of the wavelet function $\psi_{a,b}(t)$.

In order to obtain the common periods between two time series, the cross-wavelet transform (XWT) can be used (Bolzan & Rosa, 2012). The XWT is given by (Grinsted et al., 2004):

$$XWT^{xy}(a,b) = W^y(a,b)W^x(a,b)^*, \quad (4)$$

where W^x and W^y represent the WT applied on the time series $x(t)$ and $y(t)$, respectively and (*) represents the complex conjugate of the WT.

The global wavelet spectrum (GWS) is used to precisely identify the most energetic periods present in a time series in the WT analysis, as well as the main periods where the correlation between the two time series is higher in the XWT analysis. The GWS is given by the following equations:

$$GWS_{WT} = \int \left|WT(a,b)\right|^2 db \quad (5)$$

and

$$GWS_{XWT} = \frac{\sigma^x\sigma^y}{\sigma^x + \sigma^y}\int \left|W^{yx}(a,b)\right|^2 db, \quad (6)$$

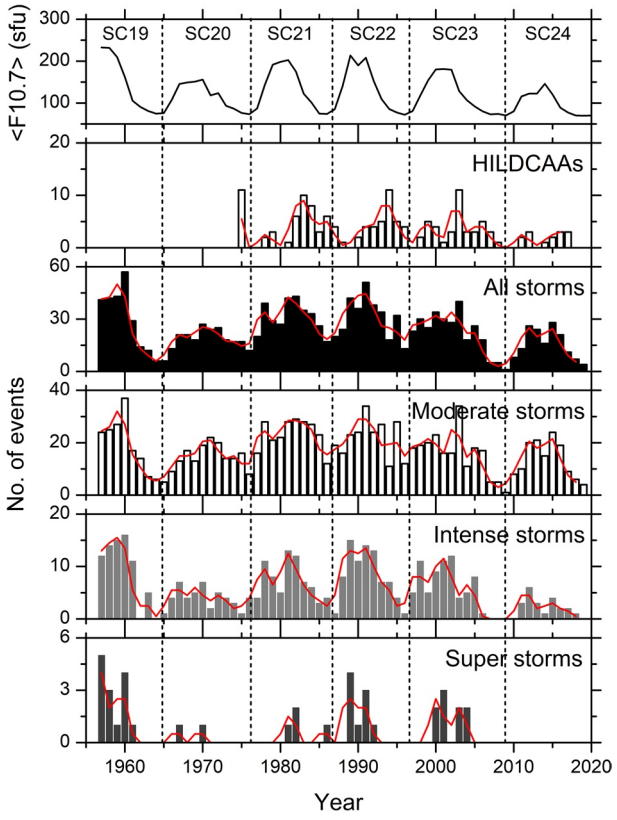

Figure 2. From top to bottom, the panels show the yearly mean F10.7 solar fluxes, the yearly numbers of HILDCAAs, all geomagnetic storms, moderate storms, intense storms, and super storms, respectively. Superposed red curves in the panels two–six show the 2-year moving averages. The starting and the ending times of each solar cycle are shown by the dashed vertical lines. Numbers of the cycles are shown on the top panel.

where GWS_{WT} represents the GWS for the WT analysis and GWS_{XWT} for the XWT analysis. σ^x and σ^y in Equation 6 represent the variances of $x(t)$ and $y(t)$, respectively.

2.5. Data Sources

The geomagnetic Dst (1 h), ap (3 h), and AE (1 min) indices are collected from the World Data Center for Geomagnetism, Kyoto, Japan (http://wdc.kugi.kyoto-u.ac.jp/). The 1 h resolution solar wind plasma and IMF data are obtained from the OMNIWeb (http://omniweb.gsfc.nasa.gov/). The OMNI database is formed by time-shifting the solar/interplanetary measurements by the NASA's Advanced Composition Explorer (ACE), Wind and Interplanetary Monitoring Platform 8 (IMP 8) spacecraft to the Earth's bow shock. The IMF vector components in geocentric solar magnetospheric (GSM) coordinates are used in this work. In the GSM coordinates, the x-axis is directed toward the Sun, and the y-axis is in the $\mathbf{\Omega} \times \hat{\mathbf{x}} / | \mathbf{\Omega} \times \hat{\mathbf{x}} |$ direction, where $\mathbf{\Omega}$ is aligned with the magnetic south pole axis of the Earth. The z-axis completes a right-hand system.

3. Results

3.1. Solar Cycle Variation of HILDCAAs, Geomagnetic Storms, and Geomagnetic Activity Indices

Figure 2 shows the variations of the yearly mean F10.7 solar flux (<F10.7>) as well as the yearly numbers of HILDCAAs and geomagnetic storms of varying intensity under this study. The solar cycle (SC) numbers, from SC19 through SC24, are marked on the top panel. As can be noted from the <F10.7> variation, the study interval spans from the maximum of SC19 to the end of SC24 – ~5.5 solar cycles. The peak <F10.7> fluxes in sfu (and approximate duration in year) for the cycles SC19 through SC24 are: ~233 (10.5), ~156 (11.4), ~203 (10.4), ~213 (9.9), ~181 (12.2), ~146 sfu (11.6 years), respectively. Here, 1 sfu (solar flux unit) = 10^{-22} Wm^{-2} Hz^{-1}. Based on the peak <F10.7> values, SC19 is the strongest, and SC24 is the weakest among the cycles in the modern space exploration era, i.e., after 1957 (see Hajra, 2021, for a detailed analysis of SC24). It may be mentioned that the reduction in solar activity is attributed to a steady decline of the solar photospheric magnetic fields (at solar latitudes ≥45°) since ~1995 (see, e.g., Janardhan et al., 2010, 2015; Livingston et al., 2012; Sasikumar Raja et al., 2019; Tsurutani et al., 2011, and references therein). We classify SC20 and SC24 as the "weak cycles" (average <F10.7> peak ~151 sfu), and SC19, SC21, SC22 and SC23 as the "strong cycles" (average <F10.7> peak ~207 sfu).

The number of the geomagnetic events in each solar cycle exhibits a clear correlation with the peak <F10.7> during the cycle (Figure 2). From SC21 through SC24, the yearly HILDCAA occurrence rates (i.e., the numbers of HILDCAAs per year of observation) are ~3.5, ~4.0, ~3.4, and ~1.6, respectively. They exhibit a high correlation coefficient $r = 0.96$ with the solar cycle peak <F10.7>. The yearly storm occurrence rates for SC19 through SC24 are ~30.5, ~18.8, ~29.4, ~30.8, ~23.5, and ~14.5, respectively, exhibiting a correlation coefficient of $r = 0.96$ with the peak <F10.7>. For the moderate, intense, and super storms, the correlation coefficients (r) are 0.87, 0.99, and 0.87, respectively. Thus, the solar cycle <F10.7> magnitude largely controls the occurrence rates of the magnetic storms and HILDCAAs in a solar cycle. It is interesting to note that while SC24 had a comparable <F10.7> peak value to SC20, the number of the intense storms was remarkably low, and there was no super storms in SC24. The number of HILDCAAs also decreased drastically in SC24. Thus, SC24 is the weakest in terms of geomagnetic activity as well.

Table 1
Comparison Between the "Strong" (SC19, SC21, SC22, and SC23) and "Weak" (SC20 and SC24) Solar Cycles

	Average for "strong cycles"	Average for "weak cycles"
<F10.7> peak (sfu)	207	151
HILDCAAs (year^{-1})	4	2
All storms (year^{-1})	29	17
Moderate storms (year^{-1})	20	14
Intense storms (year^{-1})	8	3
Super storms (year^{-1})	1.0	0.1
<Dst> peak (nT)	−26	−16
<ap> peak (nT)	29	19
<AE> peak (nT)	343	249
<Bo> peak (nT)	9	7
<Vsw> peak (km s^{-1})	516	490
D500 peak (%)	64	57
<VBs> peak (mV m^{-1})	0.43	0.36
<ϵ> peak (10^{11} W)	2.68	1.69

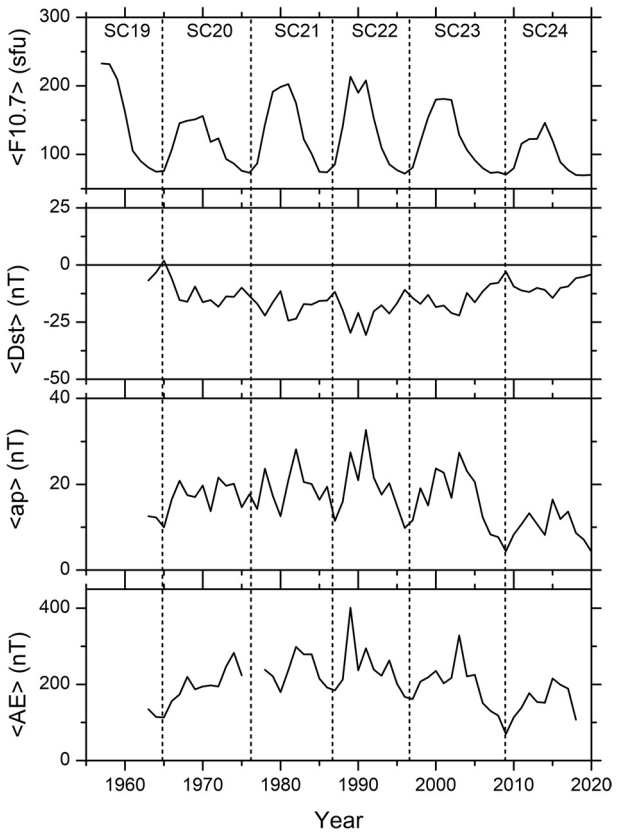

Figure 3. From top to bottom, the panels show the yearly mean F10.7 solar fluxes, and the Dst, ap, and AE indices, respectively. The starting and the ending times of each solar cycle are shown by the dashed vertical lines. Numbers of the cycles are shown on the top panel.

Table 1 shows the occurrence rates of HILDCAAs and magnetic storms of varying intensity during the weak and strong cycles. An ∼27% reduction in the <F10.7> peak is associated with ∼57% reduction in the HILDCAA occurrence rate, ∼42% reduction in all storms, ∼32% reduction in the moderate storms, ∼61% reduction in the intense storms, and ∼90% reduction in the super storms during the weak solar cycles compared to the strong cycles.

In each solar cycle, HILDCAAs and magnetic storms can occur at any phase (Figure 2). However, the HILDCAA occurrence peaks around the descending phase. On the other hand, the storm occurrence is more centered around the solar maximum. When storms are separated in intensity, the solar maximum centric occurrence is most prominent for the intense storms, while the moderate storms peak during the descending phase, resulting in an overall dual-peak occurrence pattern of the magnetic storms. These results are consistent with previous reports (e.g., Echer et al., 2008, 2011; Hajra et al., 2013) and attributed to various solar/interplanetary sources of HILDCAAs and magnetic storms (see, e.g., Du, 2011; Du & Wang, 2012; Echer et al., 2004, 2008, 2011; Gonzalez et al., 1990, 1994, 2011; Hajra et al., 2013, 2014, 2020; Kirov et al., 2013; Samsonov et al., 2019; Tsurutani & Gonzalez, 1987; Veretenenko et al., 2020, and references therein, for a more detailed discussion of this topic).

Figure 3 shows the variations of the yearly mean geomagnetic activity indices Dst (<Dst>), ap (<ap>), and AE (<AE>). <F10.7> is repeated from Figure 2 for a reference to the solar cycle (marked on the top panel). The variations of the indices confirm a weaker geomagnetic activity strength during SC20 and SC24 (weak cycles) compared to that during SC21, SC22 and SC23 (strong cycles). According to Table 1, the solar cycle peak values of the indices <Dst>, <ap>, and <AE> exhibit reductions by ∼36%, ∼35%, and ∼27%, respectively during the weak cycles with respect to their values during the strong cycles.

In addition, the geomagnetic activity index averages are quite lower for the weakest cycle 24 (peak <Dst> ∼ −14 nT, <ap> ∼ 16 nT, and <AE> ∼ 216 nT) than even for the equally weak cycle 20 (peak <Dst> ∼ −18 nT, <ap> ∼ 22 nT, and <AE> ∼ 283 nT).

To study the long-term dependence of the geomagnetic events and the geomagnetic indices on the solar cycle, the time-lagged cross-correlation analysis is performed using the yearly mean values of the F10.7 solar flux, the geomagnetic indices, and the yearly numbers of HILDCAAs and magnetic storms. The results are shown in Figure 4. Correlation between HILDCAAs and <F10.7> peaks ($r = 0.59$) at a time lag of ∼3 years. This is consistent with the HILDCAA occurrence peaking in the descending phase of the solar cycle (Figure 2).

While all the storms together (AS) exhibit a correlation coefficient $r = 0.73$ with <F10.7> at a zero time lag, variations can be noted for storms with varying intensity (Figure 4). Correlation of the moderate storms ($r = 0.65$) peaks at ∼1-year lag, and correlations of the intense ($r = 0.78$) and super ($r = 0.58$) storms peak at a zero time lag.

The geomagnetic indices <ap> and <AE> exhibit significant positive correlations of $r = 0.60$ with 0.57 at the time lags of 0 and 1 year, respectively with <F10.7>. However, the <Dst> index is anti-correlated ($r = -0.66$) to <F10.7> at the zero time lag.

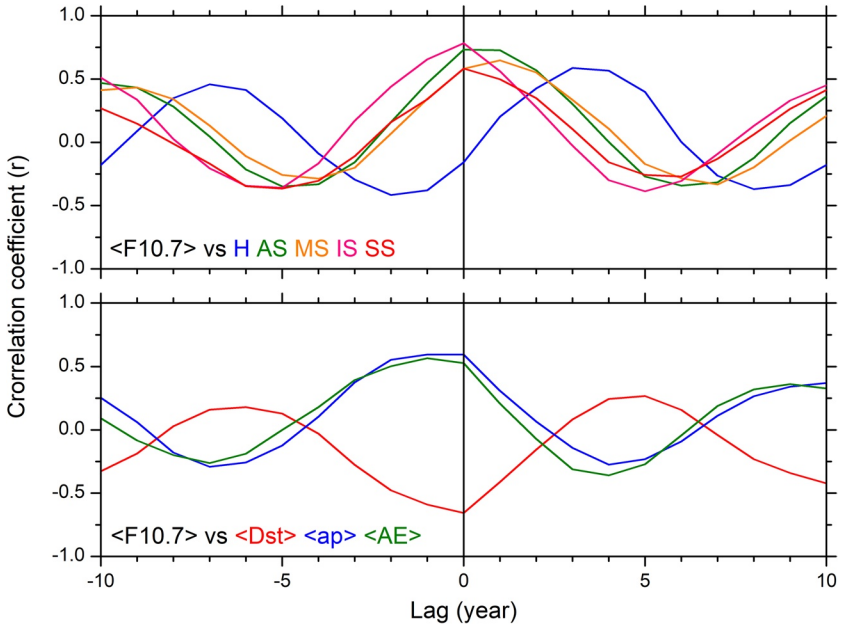

Figure 4. Time-lagged cross-correlation analysis of the geomagnetic events and geomagnetic indices with the <F10.7> solar flux. The top panel corresponds to HILDCAAs (H), all magnetic storms (AS), moderate storms (MS), intense storms (IS), and super storms (SS). The bottom panel corresponds to the <Dst>, <ap> ,and <AE> indices.

3.2. Solar Wind-Magnetosphere Coupling

The solar wind plasma and IMF are explored to study the solar wind-magnetosphere coupling processes, leading to the geomagnetic activity variations described in Section 3.1. Figure 5 shows the variations of the yearly mean IMF magnitude Bo (<Bo>), solar wind speed Vsw (<Vsw>), D500, coupling function VBs (<VBs>), and Akasofu ϵ-parameter (<ϵ>). <F10.7> is repeated from Figure 2.

The IMF <Bo>, <VBs>, and <ϵ>-parameter are organized with the solar cycle—increasing and decreasing with the increases and decreases in <F10.7>, respectively (Figure 5). The solar cycle peaks of <Bo>, <VBs>, and <ϵ> -parameter are correlated with the <F10.7> peaks. On the other hand, the <Vsw> and D500 peaks are observed during the solar cycle descending phase. The solar/interplanetary parameter variations indicate the weakest solar wind-magnetosphere coupling in SC24.

The solar cycle peaks of the IMF magnitude and the solar wind-magnetosphere coupling functions during the weak and strong cycles are listed in Table 1. The weak cycles exhibit ~23% decrease in <Bo>, ~5% decrease in <Vsw>, ~10% decrease in D500, ~17% decrease in <VBs>, and ~37% decrease in <ϵ> -parameter compared to those during the strong cycles. The results clearly show, quantitatively, that the weak solar cycles have not only the lower peaks of <F10.7> but also the decreased values of the solar wind-magnetosphere coupling. The later resulted in the weaker geomagnetic activity indices and lower occurrence rates of HILDCAAs and magnetic storms during the weak cycles compared to the strong ones.

The time-lagged cross-correlation analysis of the HILDCAAs, geomagnetic storms and geomagnetic indices with the IMF and solar wind parameters is performed to study the time variation of their relationships. The results are shown in Figure 6 and are summarized in Table 2.

The HILDCAA occurrence rate exhibits the strongest correlation with <Vsw> (r = 0.78) and D500 (r = 0.74) at the zero time lag. This result confirms a strong association of HILDCAAs with HSSs. However, the correlations of HILDCAAs with <Bo> (r = 0.51), <VBs> (r = 0.46), and <ϵ> (r = 0.52) are weaker, and they peak at the time lags of ~3, ~3, and ~2 years, respectively. On the other hand, the geomagnetic storms, from moderate to intense, are strongly correlated with <Bo> and solar wind-magnetosphere coupling functions at the zero time lag. There is no significant correlation between the magnetic storms and <Vsw> or D500.

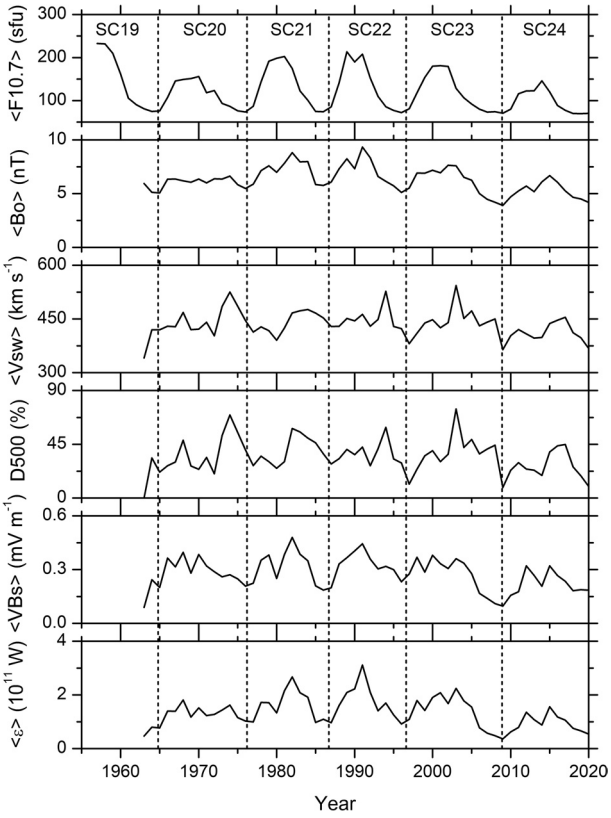

Figure 5. From top to bottom, the panels show the yearly mean F10.7 solar fluxes, IMF Bo, Vsw, D500, VBs, and Akasofu ϵ-parameter, respectively. The starting and the ending times of each solar cycle are shown by the dashed vertical lines. Numbers of the cycles are shown on the top panel.

The geomagnetic indices <Dst>, <ap>, and <AE> exhibit significant correlation with <Bo>, <VBs>, and <ϵ>. While <AE> shows some association with <Vsw> and D500, correlations of <Dst> and <ap> with <Vsw> and D500 are poor.

3.3. Long-Term Trends in Solar and Geomagnetic Activity: Wavelet and Cross-Wavelet Analyses

The aim of this section is to investigate the long-term trends (periodicity) in the geomagnetic activity and the driving solar and interplanetary parameters. Figure 7 shows the representative wavelet analysis of the yearly mean F10.7 and Vsw. From the <F10.7> wavelet spectrum periodogram (Figure 7 [middle panel]), a strong power can be seen concentrated around the 10–11-year period inside the "cone of influence." As the "edge effect" may be significant outside the cone of influence, any period observed outside this region is ignored. The wavelet periodogram shows a continuous energy distribution around the 10–11-year period during the entire interval of the study. The global wavelet spectrum shows the highest amplitude precisely at the ~10.9-year period.

The wavelet spectrum of <Vsw> is comparatively more complex with additional periods (Figure 7 [bottom panel]). Several significant periods (with strong power) are recorded inside the cone of influence. More precisely, from the corresponding global wavelet spectrum, ~9.8-year period has the strongest amplitude, followed by the amplitudes of ~16.2-, ~4.4-, and ~2.5-year periods (in the decreasing order of amplitude). The ~9.8 and ~16.2-year periods have the continuous distribution in time. On the other hand, the period of ~4.4 years has a quasi-continuous distribution, and the ~2.5-year period has an intermittent distribution, where the regions with higher energy are during the solar cycle descending phase. The complex spectrum of <Vsw> may be indicative of the multiple origins of the fast solar winds, namely, HSSs from the coronal holes (Bame et al., 1993; Burlaga et al., 1978; Krieger et al., 1973; Sheeley & Harvey, 1981), the interplanetary coronal mass ejections (ICMEs: Illing & Hundhausen, 1986; Odstrčil & Pizzo, 1999; Palmerio et al., 2018; Yurchyshyn et al., 2007), and the shocked solar wind behind the interplanetary shocks (Kennel et al., 1985; Tsurutani et al., 1988).

Similar wavelet analysis is performed for the IMF <Bo>, D500, <VBs>, <ϵ>-parameter, HILDCAAs, and geomagnetic storms of varying intensity, as well as for the geomagnetic indices <Dst>, <ap> and <AE>. The results are summarized in Table 3. All of the solar and interplanetary parameters have a common periodicity of ~10–11 years, which has a source in the solar cycle. Additional, significant (inside the cone of influence) periods of ~15–16 years and ~3–5 years are suggested to be induced by <Vsw> or D500.

Table 2
The Peak Time-Lagged Cross-Correlation Coefficients

	HILDCAA	AS	MS	IS	SS	<Dst>	<ap>	<AE>
<Bo>	0.51 (3)	0.89 (0)	0.78 (0)	0.85 (0)	0.55 (0)	−0.82 (0)	0.84 (0)	0.81 (0)
<Vsw>	0.78 (0)	0.38 (−3)	0.35 (9)	0.37 (−2)	0.24 (−2)	−0.41 (0)	0.54 (0)	0.66 (0)
D500	0.74 (0)	0.37 (−2)	0.39 (9)	0.36 (−1)	0.34 (7)	−0.39 (−1)	0.51 (0)	0.64 (0)
<VBs>	0.46 (3)	0.82 (0)	0.73 (0)	0.75 (0)	0.56 (0)	−0.73 (0)	0.79 (0)	0.70 (0)
<ϵ>	0.52 (2)	0.88 (0)	0.76 (0)	0.83 (0)	0.64 (0)	−0.83 (0)	0.90 (0)	0.81 (0)

Note: Numbers in the parentheses are the time lags in year.

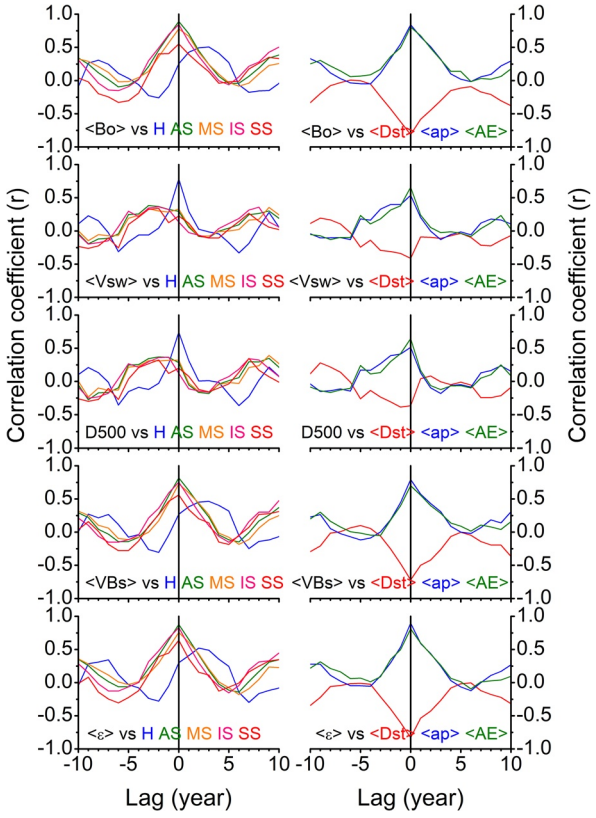

Figure 6. Time-lagged cross-correlation analysis of the geomagnetic event numbers and the geomagnetic indices with the IMF and solar wind parameters. The left panels correspond to the yearly numbers of HILDCAAs (H), all storms (AS), moderate storms (MS), intense storms (IS), and super storms (SS), while the right panels correspond to the geomagnetic indices <Dst>, <ap>, and <AE>. The panels from the top to bottom correspond to the IMF <Bo>, <Vsw>, D500, <VBs>, and <ϵ> -parameter, respectively.

Table 3
Wavelet Analysis Result

	Periods (year)
<F10.7>	10.9
<Bo>	10.9
<Vsw>	9.8, 16.2, 4.4, 2.5
D500	10.3, 15.3, 4.5, 2.5
<VBs>	11.1
<ϵ>	10.9
HILDCAA	10.0, 4.1
All storm	11.0, 2.7
Moderate storm	10.9, 2.5
Intense storm	11.0, 3.4
Super storm	10.9, 15.4, 3.2
<Dst>	10.8, 5.3
<ap>	10.9
<AE>	11.4, 14.4, 7.7, 5.3, 2.5

Note: The periods are arranged in the descending order of amplitude.

In addition to the ~10–11-year period, HILDCAAs exhibit a significant period of ~4 years, and the geomagnetic storms exhibit the secondary periods of ~15 and ~3 years. The <Dst> index has an additional period of ~5 years, and <AE> exhibits the periods of ~14, ~8, ~5, and ~3 years in addition to the ~11-year period. The ~3–5-year period is attributed to the dual-peak solar cycle variation (Clúa de Gonzalez et al., 1993; Gonzalez et al., 1990), and the ~16–18-year period to the coronal hole topology variation (Makarov & Sivaraman, 1989).

In order to identify the sources of the periodic variations of the geomagnetic activity, the cross-wavelet analysis is performed between the geomagnetic activity, and the solar and interplanetary parameters. Figure 8 shows the cross-wavelet analysis between HILDCAAs and <F10.7> (top panel) and between HILDCAAs and <Vsw> (bottom panel). The common periods in each case are shown in the corresponding global wavelet spectra on the right. As expected, the HILDCAAs versus <F10.7> cross-wavelet spectrum (as well as the corresponding global wavelet spectrum) reveals a significant ~10-year period. The ~9.9-year period in the HILDCAAs versus <Vsw> cross-wavelet spectrum has a source in the solar cycle (remember that HILDCAAs are not in phase with the <F10.7> variation). An additional ~4-year common period is confirmed between HILDCAAs and <Vsw>.

Figure 9 shows the cross-wavelet analysis of all storms with <F10.7> and <Vsw>. As in case of the HILDCAAs (Figure 8), while the ~11-year periodicity in the storms is correlated with that in <F10.7>, the <Vsw> variations induce a shorter period of ~4 years, however, with a smaller amplitude.

4. Summary

We presented an up-to-date long-term database of the magnetic storms and HILDCAAs using all available geomagnetic Dst (1 h resolution) and AE (1 min) indices. The yearly variations of the geomagnetic events are used to explore the statistical characteristics of the geomagnetic activity for more than five solar cycles. The results are compared with the long-term trends in the driving solar wind-magnetosphere coupling. In addition, the solar wind-magnetosphere coupling and the geomagnetic activity are compared between the weak and strong solar cycles. The main results are summarized below.

1. The occurrence rates of the HILDCAAs and the geomagnetic storms are strongly correlated with the peak F10.7 solar cycle magnitude.
2. The magnetic storms of varying intensity exhibit a strong correlation ($r = 0.58-0.78$) with the yearly mean F10.7 solar flux at the 0−1-year time lag. This result is consistent with the storm occurrence centered around the solar cycle maximum, with a secondary peak following the solar maximum due to the moderate storms. HILDCAAs exhibit a weaker correlation ($r = 0.59$) with F10.7 at a time lag of ~3 years. This is consistent with the HILDCAA occurrence peaking around the descending phase of the solar cycle.
3. HILDCAAs exhibit the strongest correlation with Vsw ($r = 0.78$) and D500 ($r = 0.74$) at the zero time lag, indicating the most important role of the solar wind HSSs in causing the HILDCAAs. The correlations of HILDCAAs with the IMF Bo ($r = 0.51$), VBs ($r = 0.46$), and Akasofu ϵ-parameter ($r = 0.52$) are weaker, and they peak at the time lags of ~2−3 years.

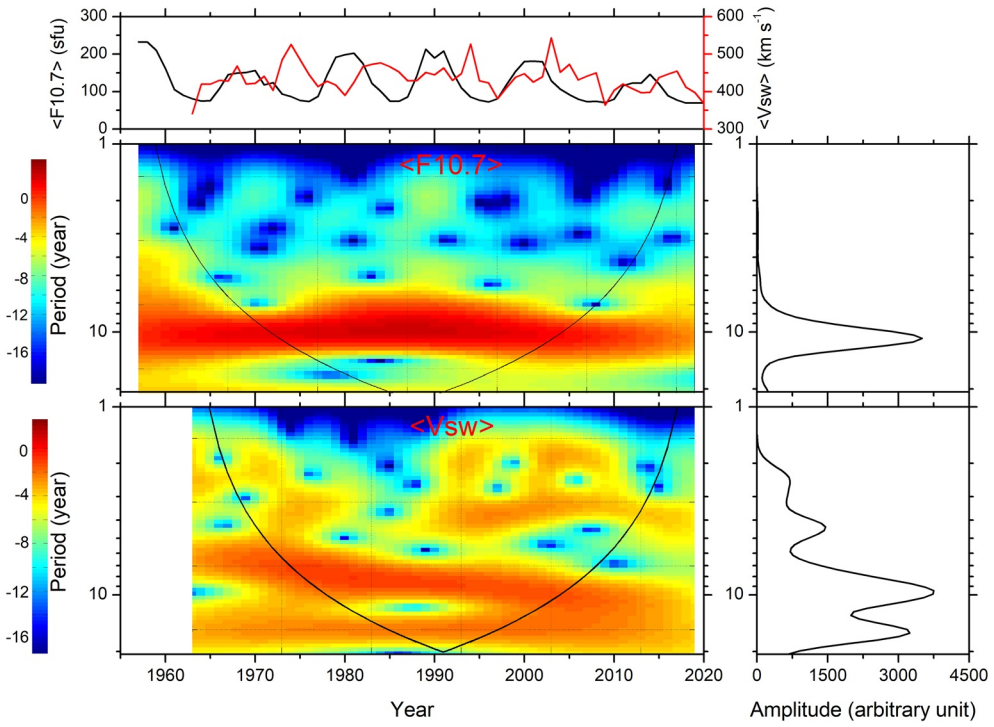

Figure 7. Wavelet analysis of <F10.7> and <Vsw>. The top panel shows the yearly variations of <F10.7> (black curve, legend on the left) and Vsw (red curve, legend on the right). The middle and the bottom panels show the wavelet spectrum periodograms of <F10.7> and <Vsw>, respectively. The cone of influence is shown by the black curve in the wavelet panels. The color bars on the left indicate the wavelet spectral power of the observed periods in arbitrary units. Panels on the right show the global wavelet spectrum indicating the significant periods.

4. The geomagnetic storms, from moderate to intense, exhibit significantly high correlations with the IMF Bo ($r = 0.78–0.89$), VBs ($r = 0.73–0.82$), and ε ($r = 0.76–0.88$) at the zero time lag. They exhibit very weak correlation with Vsw or D500.
5. The geomagnetic storm and HILDCAA occurrence rates, the geomagnetic activity indices, the solar wind and interplanetary parameters exhibit a dominating ~10-11-year periodicity. This is attributed to the ~11-year solar cycle variation. However, not all of these parameters are in phase with the solar cycle.
6. The solar wind Vsw and D500 exhibit periodicities of ~15–16 and ~3–5 years. They induce ~4-year period in HILDCAAs, ~3-year period in the magnetic storms, ~5-year period in Dst, and ~5 and ~14-year periods in AE.
7. The solar cycles 20 and 24 are not only weaker in the F10.7 solar flux peak (average ~151 sfu) than the cycles 19, 21, 22, and 23 (average ~207 sfu) but also are characterized by significantly weaker (5% − 37%) solar wind-magnetosphere coupling resulting in the reduced numbers of HILDCAAs (~57%) and magnetic storms (~32%−90%).
8. The recently complete solar cycle 24 is found to be the weakest of the cycles in the space exploration era, with the lowest solar flux peak (~146 sfu), the reduced IMF, solar wind plasma speed and solar wind-magnetosphere energy coupling compared to the previous cycles. These resulted in the lowest numbers of HILDCAAs and geomagnetic storms compared to the previous solar cycles and no super storms in solar cycle 24.

5. Discussion and Conclusions

From the study of the long and updated database of HILDCAAs, magnetic storms and solar/interplanetary data, it is concluded that the solar cycle magnitude has a strong modulation on the solar wind-magnetosphere energy coupling and the resultant geomagnetic activity. The solar cycle phase dependencies of the HILDCAAs and magnetic storms are in good agreement with the previous reported results (e.g., Clúa de

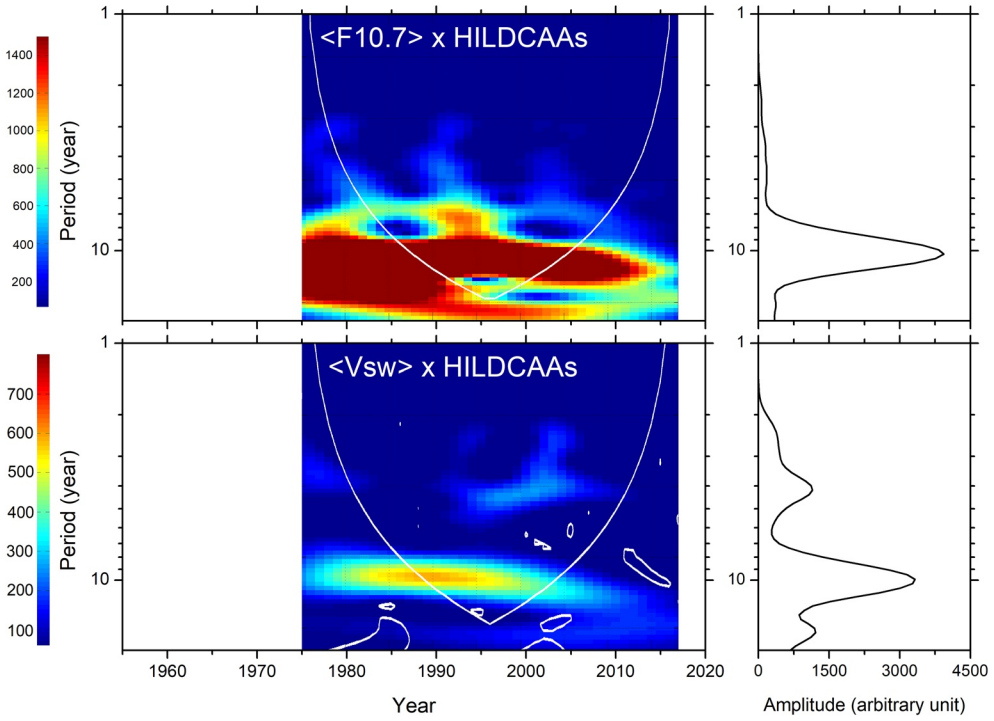

Figure 8. Cross-wavelet analysis of HILDCAAs with <F10.7> and <Vsw>. The cone of influence is shown by the white curve in each panel. The color bars on the left indicate the wavelet spectral power of the observed periods in arbitrary units. Panels on the right show the global wavelet spectrum indicating the significant common periods.

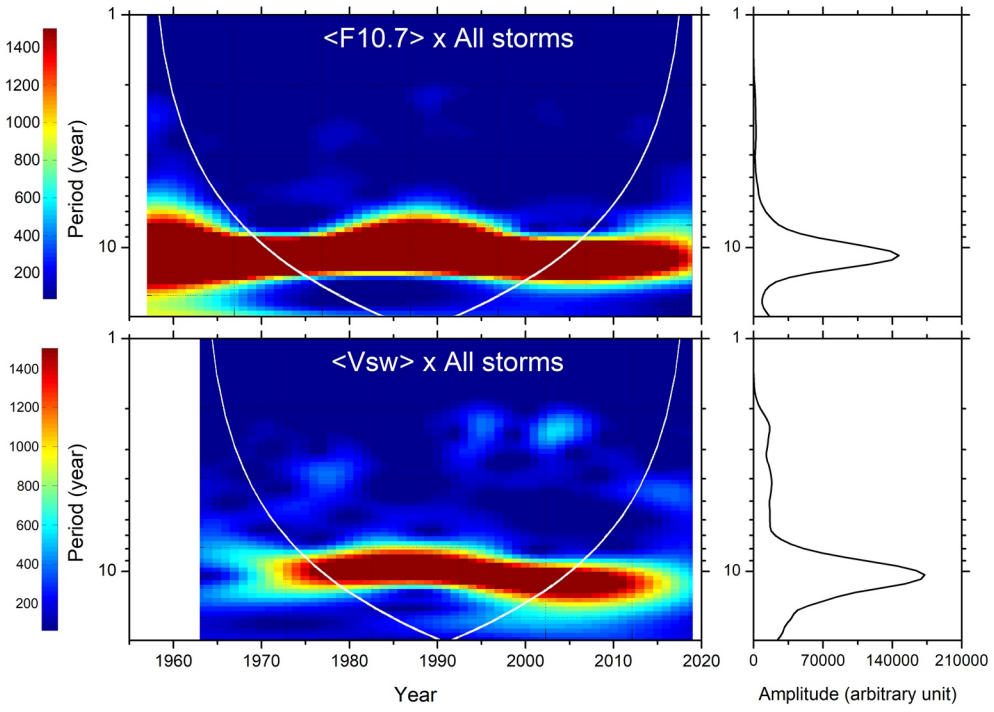

Figure 9. Cross-wavelet analysis of all magnetic storms with <F10.7> and <Vsw>. The cone of influence is shown by the white curve in each panel. The color bars on the left indicate the wavelet spectral power of the observed periods in arbitrary units. Panels on the right show the global wavelet spectrum indicating the significant common periods.

Gonzalez et al., 1993; Echer et al., 2004, 2008, 2011; Gonzalez et al., 2011; Hajra et al., 2013, 2014; Rawat et al., 2018, and references therein). Presence of the ~11-year periodicity in the solar wind-magnetosphere coupling and the geomagnetic activity confirms that the space climate is dominated by the solar cycle variation. The fast solar winds have also pronounced impact on the space climate as can be seen in the additional longer (~15–16 years) and shorter (~3–5 years) time scale variations of the geomagnetic activity.

In the space exploration era (i.e., after 1957), the solar activity cycles 20 and 24 are found to be significantly weaker than the cycles 19, 21, 22, and 23. They broadly define the space climatology. It was shown that the solar wind parameters and the consequent magnetospheric response are different in these two cycle groups. The weaker solar magnetic field leads to a lower IMF magnitude, a lower solar wind pressure and a lesser solar wind kinetic energy available for driving the magnetospheric activity. As a consequence, the numbers of the magnetic storms and HILDCAAs as well as the average geomagnetic activity decrease from the strong to the weak solar cycles.

The recently complete solar cycle 24 is found to be very weak in terms of the solar and magnetospheric activity. There have been some studies that have predicted a trend for the solar activity entering in a period of a grand minimum or a Dalton type minimum (e.g., Gonçalves et al., 2020; Jiang & Cao, 2018; Upton & Hathaway, 2018; Wang, 2017, and references therein). If this really occurs, the weak cycle 24 leads us to expect a much lower solar wind energy input in the magnetosphere, and as a consequence a significant decrease in the geomagnetic activity. This has large impacts on the space weather effects and technological applications. On the other hand, a reduced solar activity will cause a higher flux of cosmic rays in the near-Earth space, which can largely impact the manned missions at the low-Earth orbit or to the Moon and Mars. Finally, the lists of the magnetic storms and HILDCAAs compiled in this work might be of interest to the space weather researchers.

Data Availability Statement

The solar wind plasma and IMF data used in this work are obtained from the OMNI website (https://omniweb.gsfc.nasa.gov/). The geomagnetic indices are obtained from the World Data Center for Geomagnetism, Kyoto, Japan (http://wdc.kugi.kyoto-u.ac.jp/). The lists of the magnetic storms and HILDCAAs compiled in this work can be accessed through: https://doi.org/10.26022/IEDA/111826.

Acknowledgments
The work of R. Hajra is funded by the Science and Engineering Research Board (SERB: grant no. SB/S2/RJN-080/2018), a statutory body of the Department of Science and Technology (DST), Government of India, through Ramanujan Fellowship. A. M. S. Franco would like to thank CNPq (contract no. PQ-300969/2020-1, PQ-301542/2021-0) for the support. E. Echer would like to thank Brazilian agencies for research Grants: CNPq (contract no. PQ-302583/2015-7, PQ-301883/2019-0) and FAPESP (contract no. 2018/21657-1). The work of M. J. A. Bolzan was supported by CNPq agency (contract no. PQ-302330/2015-1, PQ-305692/2018-6) and FAPEG agency (contract no. 2012.1026.7000905).

References

Akasofu, S.-I. (1964). The development of the auroral substorm. *Planetary and Space Science*, *12*, 273–282. https://doi.org/10.1016/0032-0633(64)90151-5

Axford, W. I., & Hines, C. O. (1961). A unifying theory of high-latitude geophysical phenomena and geomagnetic storms. *Canadian Journal of Physics*, *39*(10), 1433–1464. https://doi.org/10.1139/p61-172

Bame, S. J., Goldstein, B. E., Gosling, J. T., Harvey, J. W., McComas, D. J., Neugebauer, M., & Phillips, J. L. (1993). Ulysses observations of a recurrent high speed solar wind stream and the heliomagnetic streamer belt. *Geophysical Research Letters*, *20*, 2323–2326. https://doi.org/10.1029/93GL02630

Bolzan, M. J. A., & Rosa, R. R. (2012). Multifractal analysis of interplanetary magnetic field obtained during CME events. *Annales Geophysicae*, *30*, 1107–1112. https://doi.org/10.5194/angeo-30-1107-2012

Burlaga, L. F., Ness, N. F., Mariani, F., Bavassano, B., Villante, U., Rosenbauer, H., et al. (1978). Magnetic fields and flows between 1 and 0.3 au during the primary mission of helios 1. *Journal of Geophysical Research*, *83*(A11), 5167–5174. https://doi.org/10.1029/JA083iA11p05167

Burton, R. K., McPherron, R. L., & Russell, C. T. (1975). An empirical relationship between interplanetary conditions and Dst. *Journal of Geophysical Research*, *80*, 4204–4214. https://doi.org/10.1029/JA080i031p04204

Cannon, P., Angling, M., Barclay, L., Curry, C., Dyer, C., Edwards, R., et al. (2013). *Extreme space weather: Impacts on engineered systems and infrastructure (Tech. Rep.)*. London: Royal Academy of Engineering. Retrieved from www.raeng.org.uk/spaceweather

Chapman, S., & Bartels, J. (1940). Geomagnetism (Vol. 1). Oxford University Press.

Chapman, S., & Ferraro, V. C. A. (1931). A new theory of magnetic storms. *Journal of Geophysical Research*, *36*, 77–97. https://doi.org/10.1029/TE036i002p00077

Clúa de Gonzalez, A. L., Gonzalez, W. D., Dutra, S. L. G., & Tsurutani, B. T. (1993). Periodic variation in the geomagnetic activity: A study based on the ap index. *Journal of Geophysical Research*, *98*, 9215–9231. https://doi.org/10.1029/92JA02200

Daglis, I. A., Thorne, R. M., Baumjohann, W., & Orsini, S. (1999). The terrestrial ring current: Origin, formation, and decay. *Rev. Geophys.*, *37*, 407–438. https://doi.org/10.1029/1999RG900009

Davis, J. C. (2002). *Statistics and data analysis in geology*. Wiley.

Davis, T. N., & Sugiura, M. (1966). Auroral electrojet activity index AE and its universal time variations. *Journal of Geophysical Research*, *71*, 785–801. https://doi.org/10.1029/JZ071i003p00785

Dungey, J. W. (1961). Interplanetary magnetic field and the auroral zones. *Physical Review Letters*, *6*, 47–48. https://doi.org/10.1103/PhysRevLett.6.47

Du, Z. L. (2011). The correlation between solar and geomagnetic activity - Part 2: Long-term trends. *Annales Geophysicae*, *29*(8), 1341–1348. https://doi.org/10.5194/angeo-29-1341-2011

Du, Z.-L., & Wang, H.-N. (2012). The relationships of solar flares with both sunspot and geomagnetic activity. *Research in Astronomy and Astrophysics*, *12*, 400–410. https://doi.org/10.1088/1674-4527/12/4/004

Echer, E., Gonzalez, W. D., Gonzalez, A. L. C., Prestes, A., Vieira, L. E. A., Dal Lago, A., et al. (2004). Long-term correlation between solar and geomagnetic activity. *Journal of Atmospheric and Solar-Terrestrial Physics*, *66*, 1019–1025. https://doi.org/10.1016/j.jastp.2004.03.011

Echer, E., Gonzalez, W. D., Guarnieri, F. L., Lago, A. D., & Vieira, L. E. A. (2005). Introduction to space weather. *Advances in Space Research*, *35*, 855–865. https://doi.org/10.1016/j.asr.2005.02.098

Echer, E., Gonzalez, W. D., & Tsurutani, B. T. (2011). Statistical studies of geomagnetic storms with peak Dst ≤ −50nT from 1957 to 2008. *Journal of Atmospheric and Solar-Terrestrial Physics*, *73*, 1454–1459. https://doi.org/10.1016/j.jastp.2011.04.021

Echer, E., Gonzalez, W. D., Tsurutani, B. T., & Gonzalez, A. L. C. (2008). Interplanetary conditions causing intense geomagnetic storms (Dst ≤ −100 nT) during solar cycle 23 (1996-2006). *Journal of Geophysical Research*, *113*, 1–20. https://doi.org/10.1029/2007JA012744

Finch, I. D., Lockwood, M. L., & Rouillard, A. P. (2008). Effects of solar wind magnetosphere coupling recorded at different geomagnetic latitudes: Separation of directly-driven and storage/release systems. *Geophysical Research Letters*, *35*, L21105. https://doi.org/10.1029/2008GL035399

Frank, L. A. (1967). On the extraterrestrial ring current during geomagnetic storms. *Journal of Geophysical Research*, *72*, 3753–3767. https://doi.org/10.1029/jz072i015p03753

Gleissberg, W. (1939). A long-periodic fluctuation of the sun-spot numbers. *The Observatory*, *62*, 158–159.

Gonçalves, Í. G., Echer, E., & Frigo, E. (2020). Sunspot cycle prediction using warped Gaussian process regression. *Advances in Space Research*, *65*, 677–683. https://doi.org/10.1016/j.asr.2019.11.011

González Hernández, I., Komm, R. R., Leibacher, J. W., & Leibacher, A. (2014). Solar origins of space weather and space climate: Preface. *Solar Physics*, *289*, 437–439. https://doi.org/10.1007/s11207-013-0454-x

Gonzalez, W. D., Echer, E., Tsurutani, B. T., Clúa de Gonzalez, A. L., & Dal Lago, A. (2011). Interplanetary origin of intense, superintense and extreme geomagnetic storms. *Space Science Reviews*, *158*, 69–89. https://doi.org/10.1007/s11214-010-9715-2

Gonzalez, W. D., Gonzalez, A. L. C., & Tsurutani, B. T. (1990). Dual-peak solar cycle distribution of intense geomagnetic storms. *Planetary and Space Science*, *38*, 181–187. https://doi.org/10.1016/0032-0633(90)90082-2

Gonzalez, W. D., Joselyn, J. A., Kamide, Y., Kroehl, H. W., Rostoker, G., Tsurutani, B. T., & Vasyliunas, V. M. (1994). What is a geomagnetic storm? *Journal of Geophysical Research*, *99*, 5771–5792. https://doi.org/10.1029/93JA02867

Grinsted, A., Moore, J. C., & Jevrejeva, S. (2004). Application of the cross wavelet transform and wavelet coherence to geophysical time series. *Nonlinear Processes in Geophysics*, *11*, 561–566. https://doi.org/10.5194/npg-11-561-2004

Hajra, R. (2021). Weakest solar cycle of the space age: A study on solar wind-magnetosphere energy coupling and geomagnetic activity. *Solar Physics*, *296*(2), 33. http://doi.org/10.1007/s11207-021-01774-9

Hajra, R., Echer, E., Tsurutani, B. T., & Gonzalez, W. D. (2013). Solar cycle dependence of high-intensity long-duration continuous AE activity (HILDCAA) events, relativistic electron predictors? *Journal of Geophysical Reserach: Space Physics*, *118*, 5626–5638. https://doi.org/10.1002/jgra.50530

Hajra, R., Echer, E., Tsurutani, B. T., & Gonzalez, W. D. (2014). Superposed epoch analyses of HILDCAAS and their interplanetary drivers: Solar cycle and seasonal dependences. *Journal of Atmospheric and Solar-Terrestrial Physics*, *121*, 24–31. https://doi.org/10.1016/j.jastp.2014.09.012

Hajra, R., Tsurutani, B. T., & Lakhina, G. S. (2020). The complex space weather events of 2017 September. *Astrophysical Journal*, *899*, 3. https://doi.org/10.3847/1538-4357/aba2c5

Hamilton, D. C., Gloeckler, G., Ipavich, F. M., Stüdemann, W., Wilken, B., & Kremser, G. (1988). Ring current development during the great geomagnetic storm of February 1986. *Journal of Geophysical Research*, *93*(A12), 14343–14355. https://doi.org/10.1029/JA093iA12p14343

Hathaway, D. H. (2015). The solar cycle. *Living Reviews in Solar Physics*, *12*. https://doi.org/10.1007/lrsp-2015-4

Illing, R. M. E., & Hundhausen, A. J. (1986). Disruption of a coronal streamer by an eruptive prominence and coronal mass ejection. *Journal of Geophysical Research*, *91*(A10), 10951–10960. https://doi.org/10.1029/JA091iA10p10951

Janardhan, P., Bisoi, S. K., Ananthakrishnan, S., Tokumaru, M., Fujiki, K., Jose, L., & Sridharan, R. (2015). A 20 year decline in solar photospheric magnetic fields: Inner-heliospheric signatures and possible implications. *Journal of Geophysical Research: Space Physics*, *120*, 5306–5317. https://doi.org/10.1002/2015JA021123

Janardhan, P., Bisoi, S. K., & Gosain, S. (2010). Solar polar fields during cycles 21-23: Correlation with Meridional flows. *Solar Physics*, *267*, 267–277. https://doi.org/10.1007/s11207-010-9653-x

Jiang, J., & Cao, J. (2018). Predicting solar surface large-scale magnetic field of cycle 24. *Journal of Atmospheric and Solar-Terrestrial Physics*, *176*, 34–41. https://doi.org/10.1016/j.jastp.2017.06.019

Kennel, C. F., Edmiston, J. P., & Hada, T. (1985). A quarter century of collisionless shock research. In *Collisionless shocks in the heliosphere: A tutorial review* (pp. 1–36). American Geophysical Union (AGU). https://doi.org/10.1029/GM034p0001

Kirov, B., Obridko, V. N., Georgieva, K., Nepomnyashtaya, E. V., & Shelting, B. D. (2013). Long-term variations of geomagnetic activity and their solar sources. *Geomagnetism and Aeronomy*, *53*, 813–817. https://doi.org/10.1134/S0016793213070128

Krieger, A. S., Timothy, A. F., & Roelof, E. C. (1973). A coronal hole and its identification as the source of a high velocity solar wind stream. *Solar Physics*, *29*, 505–525. https://doi.org/10.1007/BF00150828

Lakhina, G. S., Hajra, R., & Tsurutani, B. T. (2020). Geomagnetically induced currents. In H. K. Gupta (Ed.), *Encyclopedia of solid earth geophysics* (pp. 1–4). Springer International Publishing. https://doi.org/10.1007/978-3-030-10475-7245-1

Livingston, W., Penn, M. J., & Svalgaard, L. (2012). Decreasing sunspot magnetic fields explain unique 10.7 cm radio flux. *The Astrophysical Journal Letters*, *757*, L8. https://doi.org/10.1088/2041-8205/757/1/l8

Makarov, V. I., & Sivaraman, K. R. (1989). New results concerning the global solar cycle. *Solar Physics*, *123*(2), 367–380. https://doi.org/10.1007/BF00149112

Marques de Souza, A., Echer, E., Bolzan, M. J. A., & Hajra, R. (2018). Cross-correlation and cross-wavelet analyses of the solar wind IMF Bz and auroral electrojet index AE coupling during HILDCAAs. *Annales Geophysicae*, *36*, 205–211. https://doi.org/10.5194/angeo-36-205-2018

Morettin, P. A. (2014). *Ondas e ondaletas: Da análise de fourier à análise de ondaletas de séries temporais*. EDUSP.

Mursula, K., Usoskin, I. G., & Maris, G. (2007). Introduction to space climate. *Advances in Space Research*, *40*, 885–887. https://doi.org/10.1016/j.asr.2007.07.046

Nykyri, K., Bengtson, M., Angelopoulos, V., Nishimura, Y., & Wing, S. (2019). Can Enhanced Flux Loading by High-Speed Jets Lead to a Substorm? Multipoint Detection of the Christmas Day Substorm Onset at 08:17 UT, 2015. *Journal of Geophysical Research: Space Physics*, *124*, 4314–4340. https://doi.org/10.1029/2018JA026357

Odstrčil, D., & Pizzo, V. J. (1999). Three-dimensional propagation of coronal mass ejections (CMES) in a structured solar wind flow: 1. CME launched within the streamer belt. *Journal of Geophysical Research: Space Physics*, *104*, 483–492. https://doi.org/10.1029/1998JA900019

Ohtani, S.-I. (2001). Substorm trigger processes in the magnetotail: Recent observations and outstanding issues. *Space Science Reviews*, *95*, 347–359. https://doi.org/10.1023/A:1005231122496

Palmerio, E., Kilpua, E. K. J., Möstl, C., Bothmer, V., James, A. W., Green, L. M., et al. (2018). Coronal magnetic structure of earthbound CMES and in situ comparison. *Space Weather*, *16*, 442–460. https://doi.org/10.1002/2017SW001767

Perreault, P., & Akasofu, S.-I. (1978). A study of geomagnetic storms. *Geophysical Journal International*, *54*, 547–573. https://doi.org/10.1111/j.1365-246X.1978.tb05494.x

Rawat, R., Echer, E., & Gonzalez, W. D. (2018). How different are the solar wind-interplanetary conditions and the consequent geomagnetic activity during the ascending and early descending phases of the solar cycles 23 and 24? *Journal of Geophysical Research*, *123*, 6621–6638. https://doi.org/10.1029/2018JA025683

Rostoker, G. (1972). Geomagnetic indices. *Reviews of Geophysics*, *10*, 935–950. https://doi.org/10.1029/RG010i004p00935

Samsonov, A. A., Bogdanova, Y. V., Branduardi-Raymont, G., Safrankova, J., Nemecek, Z., & Park, J. S. (2019). Long-term variations in solar wind parameters, magnetopause location, and geomagnetic activity over the last five solar cycles. *Journal of Geophysical Research: Space Physics*, *124*, 4049–4063. https://doi.org/10.1029/2018JA026355

Sasikumar Raja, K., Janardhan, P., Bisoi, S. K., Ingale, M., Subramanian, P., Fujiki, K., & Maksimovic, M. (2019). Global solar magnetic field and interplanetary scintillations during the past four solar cycles. *Solar Physics*, *294*, 123–294. https://doi.org/10.1007/s11207-019-1514-7

Schwabe, H. (1844). Sonnen-beobachtungen im jahre 1843. *Astronomische Nachrichten*, *21*, 233–236. https://doi.org/10.1002/asna.18440211505

Sheeley, N. R., & Harvey, J. W. (1981). Coronal holes, solar wind streams, and geomagnetic disturbances during 1978 and 1979. *Solar Physics*, *70*, 237–249. https://doi.org/10.1007/BF00151331

Shue, J.-H., & Chao, J.-K. (2013). The role of enhanced thermal pressure in the earthward motion of the Earth's magnetopause. *Journal of Geophysical Research*, *118*, 3017–3026. https://doi.org/10.1002/jgra.50290

Singer, S. F. (1957). A new model of magnetic storms and aurorae. *EOS, Transactions American Geophysical Union*, *38*, 175–190. https://doi.org/10.1029/TR038i002p00175

Souza, A. M., Echer, E., Bolzan, M. J. A., & Hajra, R. (2016). A study on the main periodicities in interplanetary magnetic field BZ component and geomagnetic ae index during HILDCAA events using wavelet analysis. *Journal of Atmospheric and Solar-Terrestrial Physics*, *149*, 81–86. https://doi.org/10.1016/j.jastp.2016.09.006

Sugiura, M. (1964). Hourly values of equatorial dst for the IGY. *Annual International Geophysical Year*, *35*, 9.

Torrence, C., & Compo, G. P. (1998). A practical guide to wavelet analysis. *Bulletin of the American Meteorological Society*, *79*, 61–78. https://doi.org/10.1175/1520-0477(1998)079⟨0061:APGTWA⟩2.0.CO;2

Tsurutani, B. T., Echer, E., & Gonzalez, W. D. (2011). The solar and interplanetary causes of the recent minimum in geomagnetic activity (MGA23): a combination of midlatitude small coronal holes, low IMF BZ variances, low solar wind speeds and low solar magnetic fields. *Annales de Geophysique*, *29*, 839–849. https://doi.org/10.5194/angeo-29-839-2011

Tsurutani, B. T., & Gonzalez, W. D. (1987). The cause of high-intensity long-duration continuous AE activity (HILDCAAs): Interplanetary Alfvén wave trains. *Planetary and Space Science*, *35*, 405–412. https://doi.org/10.1016/0032-0633(87)90097-3

Tsurutani, B. T., Gonzalez, W. D., Tang, F., Akasofu, S. I., & Smith, E. J. (1988). Origin of interplanetary southward magnetic fields responsible for major magnetic storms near solar maximum (1978-1979). *Journal of Geophysical Research*, *93*(A8), 8519–8531. https://doi.org/10.1029/JA093iA08p08519

Tsurutani, B. T., Gonzalez, W. D., Tang, F., & Lee, Y. T. (1992). Great magnetic storms. *Geophysical Research Letters*, *19*, 73–76. https://doi.org/10.1029/91GL02783

Tsurutani, B. T., Gonzalez, W. D., Tang, F., Lee, Y. T., Okada, M., & Park, D. (1992). Reply to L. J. Lanzerotti: Solar wind ram pressure corrections and an estimation of the efficiency of viscous interaction. *Geophysical Research Letters*, *19*, 1993–1994. https://doi.org/10.1029/92GL02239

Tsurutani, B. T., Lakhina, G. S., Echer, E., Hajra, R., Nayak, C., Mannucci, A. J., & Meng, X. (2018). Comment on "Modeling Extreme 'Carrington-Type' Space Weather Events Using Three-Dimensional Global MHD Simulations" by C. M. Ngwira, A. Pulkkinen, M. M. Kuznetsova, and A. Glocer. *Journal of Geophysical Research: Space Physics*, *123*, 1388–1392. https://doi.org/10.1002/2017JA024779

Tsurutani, B. T., & Meng, C.-I. (1972). Interplanetary magnetic-field variations and substorm activity. *Journal of Geophysical Research*, *77*(16), 2964–2970. https://doi.org/10.1029/JA077i016p02964

Upton, L. A., & Hathaway, D. H. (2018). An updated solar cycle 25 prediction with aft: The modern minimum. *Geophysical Research Letters*, *45*(16), 8091–8095. https://doi.org/10.1029/2018GL078387

Veretenenko, S., Ogurtsov, M., & Obridko, V. (2020). Long-term variability in occurrence frequencies of magnetic storms with sudden and gradual commencements. *Journal of Atmospheric and Solar-Terrestrial Physics*, *205*, 105295. https://doi.org/10.1016/j.jastp.2020.105295

Wang, Y.-M. (2017). Surface flux transport and the evolution of the sun's polar fields. *Space Science Reviews*, *210*, 351–365. https://doi.org/10.1007/s11214-016-0257-0

Williams, D. J. (1987). Ring current and radiation belts. *Reviews of Geophysics*, *25*, 570–578. https://doi.org/10.1029/RG025i003p00570

Yurchyshyn, V., Hu, Q., Lepping, R. P., Lynch, B. J., & Krall, J. (2007). Orientations of LASCO Halo CMES and their connection to the flux rope structure of interplanetary CMES. *Advances in Space Research*, *40*, 1821–1826. https://doi.org/10.1016/j.asr.2007.01.059